

Radar images of rough surface scattering: Comparison of numerical and analytical models

Hyunjun Kim and Joel T. Johnson

The Ohio State University

Department of Electrical Engineering

ElectroScience Laboratory

1320 Kinnear Road, Columbus, Ohio 43212

hjk@esl.eng.ohio-state.edu

Abstract: Rough surface scattering theories are investigated through analysis of radar images. Backscatter results from 10 ~ 14 GHz under tapered wave illumination are considered for 1-D random rough surface realizations which satisfy an impedance boundary condition. Back-projection tomography is applied to form 2-D synthetic aperture radar images from deterministic surface scattered field data at multiple incidence angles and frequencies. Numerical predictions of surface backscattered fields are obtained from an accelerated forward-backward method, and the resulting images are compared with those obtained from approximate scattering theories such as the physical optics (PO) approximation, the small slope approximation (SSA) and the non-local SSA (NLSSA). The resulting radar images illustrate scattering sources associated with single and multiple scattering on the boundary, and a ray tracing analysis confirms the locations of time-delayed image points due to double reflections. For single scattering effects, images demonstrate excellent agreement between analytical and numerical methods in both horizontal and vertical polarizations. For surfaces with rms height 2.0 cm and correlation length 7.5 cm at normal incidence, multiple scattering effects are observed and successfully captured when the lowest order NLSSA is employed.

1 Introduction

In recent years extensive studies of rough surface scattering have been conducted to develop accurate and efficient models valid over a wide range of incident and scattering angles. Several analytical approaches have shown promising results for specified ranges of surface statistics [1, 2]. No approximate solution, however, clearly explains all possible scattering mechanisms, and each approximation is limited to a particular range of surface roughness or electromagnetic parameters. Evaluation of analytical theories is typically based on results for average cross sections. However, data averaged over surface realizations does not provide a detailed description of surface scattering phenomena, so that detailed investigations of the scattering physics captured by the approximate theories have not been performed. Due to the lack of information on the physical behavior of scattering from rough surfaces, a more descriptive approach can be helpful to understand the existing theories.

Imaging techniques have been widely used in other areas of electromagnetics as a tool for analysis and understanding of scattering and propagation phenomena. For example, studies of natural target scattering have used high-resolution radar images to identify small foliage targets [3–6]. Imaging techniques to assist in separating buried targets from surface clutter are also of interest in subsurface target detection problems [7, 8]. The advantages of imaging techniques for improving understanding motivate the use of high resolution imaging for studies of rough surface scattering phenomena [9].

Although computational requirements in image analysis are compounded by the need for data at multiple frequencies and aspect angles, advances in computing facilities and the recent development of efficient numerical methods for backscatter predictions enable radar image formation with numerical scattering models. Images formed from numerical scattering models can be used as a reference solution to evaluate the performance of the existing analytical models such as the small slope approximation (SSA) and the non-local SSA (NLSSA). Recent studies have proven the success of these approximations in terms of average radar cross sections and for surfaces with moderate rms slopes [10–17].

In this paper, high spatial resolution radar images of a single realization of a Gaussian random process surface are formed using both approximate and numerical surface scattering models. In

Section 2, the scattering geometry is described, and a brief review of the analytical and numerical methods to be evaluated is presented, followed by a description of the 2-D synthetic aperture radar (SAR) image formation procedure. Images from the scattering models are compared in Section 3, including a discussion of the performance of the approximate theories. A summary and conclusions are presented in Section 4.

2 Scattering geometry and background theories

A. Problem geometry and incident field

Figure 1 illustrates the scattering geometry of a typical 1-D rough surface, $z = f(x)$, described as a realization of a Gaussian random process with a Gaussian correlation function. Surface statistics can be characterized by the rms height (σ) and correlation length (l_c). The rms slope (s) of the surface is proportional to the ratio of the two parameters ($s = \sqrt{2}\sigma/l_c$) for a Gaussian spectrum. The medium is assumed to be described by an impedance boundary condition with a relative permittivity of $(39.7 + i40.2)$.

A single surface realization is used in this paper, generated with rms height 1.25 cm and correlation length 7.5 cm. A larger amplitude version of this surface is also employed by multiplying the original surface amplitude by 1.6 to obtain an rms height of 2.0 cm. The resulting rms slopes for the two surfaces become 0.236 (13.28°) and 0.377 (20.66°), respectively.

The length of the surface profile studied is $L = 1.92$ meters (64λ at 10 GHz). To avoid scattering effects from surface edges, a Gaussian “tapered wave” [18] is used as the incident field. According to the criterion described in [19], a 64λ surface with tapering parameter $g = L/5$ is sufficient to provide accurate surface scattering calculations up to the maximum 55° incidence angle considered in this paper.

Scattering cross sections under tapered wave illumination are obtained for the analytical theories through a superposition of plane wave responses with a Gaussian weighting in the spectral domain:

$$\Psi_s(k_{ix}, k_{sx}) = \frac{g}{2\sqrt{\pi}} \int_{-\infty}^{\infty} \psi_s(k_{ix} + k_x, k_{sx}) e^{-(k_x g/2)^2} dk_x, \quad (1)$$

where ψ_s is the scattered field under uniform plane wave excitation, $g = L/5$ determines the taper

size of the incident field, and k_{ix} and k_{sx} denote the wave numbers of incident and scattered fields in the x direction, respectively.

B. Scattering theories

A numerical solution based on an iterative method of moments (MOM) called the forward-backward (FB) method is used as a reference backscatter result. To improve the efficiency of the computations, the novel spectral acceleration algorithm is employed [20]. A total of 1024 points were used in sampling the surface profile and surface fields for all scattering calculations of this paper. The physical optics (PO) approximation, the small slope approximation (SSA) and the non-local SSA (NLSSA) are also investigated in terms of radar images in this paper. Results from small perturbation method (SPM) are not included in this paper because SPM is valid only for small height surfaces [1, 21].

In PO predictions, the scattering phenomena involve only single scattering on the surface neglecting interactions between points of the surface [1]. It has been shown that a PO model should be adequate for surfaces with large radii of curvature and for near specular scattering regardless of surface height. PO results however show little polarization dependence even at oblique observation angles.

The small slope approximation (SSA), proposed by Voronovich, is based on a series expansion in generalized surface slope [10–15]. Though this series gradually improves results as additional terms are included, additional integrations in higher order terms make the computations more complicated. However, SSA results have shown good agreement with exact solutions when moderate incident angles are considered (less than 45°) and when rms slopes of surfaces are relatively small (less than 30°) so that only a few series terms are required [15]. In this paper, zeroth (first order in slope) and first (second order in slope) order SSA results are considered. Note that the first order SSA requires an additional integration for backscatter computation compared to PO calculations, but remains very efficient compared to the MOM/FB solution.

The non-local SSA (NLSSA) is an improvement of the SSA which attempts to include non-local interactions more accurately [16, 17]. To include the multiple interactions explicitly, a second kind integral equation (IE) is expanded to include double scattering terms, and then the expansion in

generalized surface slope is applied. A stationary phase analysis shows that the lowest order NLSSA can capture the double scattering mechanism [16]. In the references, expressions for kernels in the NLSSA integrations were developed for PEC surfaces. Since these kernels are based on combinations of SPM solutions, the NLSSA formula for an impedance surface can be easily achieved without loss of generality. Also expressions for vertical polarization can be obtained by duality principles. In this paper, the zeroth order NLSSA formulation is employed, which also requires an additional integration compared to PO calculations. However, the NLSSA double integration can be separated into a pair of 1-D Fourier transforms so that very efficient calculations are possible.

C. Construction of radar images

A 2-D SAR image of a deterministic surface can be constructed from a set of frequency and angular swept complex backscatter field data. This corresponds to a “spotlight” SAR image in which the incident beam is oriented to illuminate a fixed surface area. Tomographic processing using an inverse Fourier transform with back projection is employed to generate the images of this paper [22,23].

For normal incidence, the down- and cross-range directions coincide with the $-z$ and $+x$ axes as shown in Figure 1, respectively (i.e., the incident field approaches the surface from above). Down- and cross-range resolutions of the image can be determined by the frequency and angular bandwidths, respectively. The down-range and cross-range resolutions, r_d and r_c , are given by

$$r_d = \frac{c}{2B}, \quad r_c = \frac{c}{2f_o \sin \Theta}, \quad (2)$$

where c is the velocity of light, and B and Θ represent the frequency bandwidth centered on f_o and the angular rotation, respectively. To resolve surface variations on the order of a wavelength, backscatter data were collected over a 4 GHz frequency bandwidth (10 - 14 GHz) and a 20° angular bandwidth corresponding 3.75 cm down- and 3.65 cm cross-range resolution in the image domain, respectively.

The unambiguous down- and cross-ranges, D_d and D_c , can be obtained by the following equations:

$$D_d = \frac{c}{2\delta f}, \quad D_c = \frac{c}{2f_o \delta \theta}, \quad (3)$$

where δf and $\delta\theta$ denote the steps in frequency and angle, respectively. Step sizes 50 MHz ($D_d = 3$ meters) and 0.2° ($D_c = 3.6$ meters at $f_o = 12$ GHz) are used so that image formation with large down range and cross range unambiguous regions are possible at normal incidence. Note that these unambiguous ranges should also take into account the possible ranges of time-delayed images due to multiple scattering.

To reduce the side-lobe level, a proper choice of windows is necessary. Since image formation is closely related to the Fourier transform, there is a tradeoff between side-lobe level and spatial resolution. Windows functions in both frequency and angle are chosen to set the relationship between these quantities. In this paper the well-known simple windows are used [24]. A rectangular window has optimum resolution, but the first side-lobe level is relatively high (-13 dB) so that minor scattering events other than strong single scattering can be completely obscured by the side-lobes. The Hamming widow has a low side-lobe level (-43 dB) with a wider main lobe. The disadvantage of the Hamming window is that the side-lobe level does not decrease significantly at wide ranges. Throughout this paper a Kaiser-Bessel window ($\alpha = 2$) is selected as an appropriate choice for the windowing function, resulting in a fast decaying side-lobe level at the expense of degrading image resolution.

3 Backscatter Results and 2-D SAR Images

A. Moderate height surface

First, SAR images of the moderate rms height surface with $\sigma = 1.25$ cm and $l_c = 7.5$ cm are investigated for aspect angles centered at normal incidence. The images in Figure 2 show the horizontal (HH) and vertical (VV) polarization images reconstructed from the exact numerical results (MOM/FB). Each image is expressed within the dynamic range of 60 dB ($-60 \sim 0$ dB) and composed of 200×200 pixels in a $2 \text{ m} \times 2 \text{ m}$ range so that the pixel size is much smaller than the image resolution (note only a $2 \text{ m} \times 1.6 \text{ m}$ range is shown in the figure). As mentioned in the previous section, the image resolution depends on the choice of windowing function as well as the angular and frequency bandwidths.

Images are observed to have a maximum scattering level at the center of the surface due to the

tapered wave illumination on the surface. The surface profile, $z = f(x)$, is also overlaid to match scattering centers to the corresponding surface points. The main scattering center distributions are from single scattering responses corresponding to the near specular points as shown in the figure. The maximum pixel amplitudes of the images are -1.18 dB and -1.23 dB for HH and VV, respectively.

Radar images obtained from the PO and SSA theories were found to be virtually identical to those in Figure 2, and thus are not plotted. PO results show maximum pixel amplitudes of -1.20 dB for HH and -1.19 dB for VV, showing very little polarization dependence as expected. Zeroth order and first order SSA images are also almost identical, and produce maximum pixel amplitudes of -1.26 and -1.30 dB for HH and VV, respectively. The maximum pixel amplitude differences between PO, first order SSA, and MOM images are thus less than 0.1 dB, demonstrating the accuracy of approximate solutions in predicting single scattering effects for this particular surface at near normal incidence.

It is also interesting to calculate image differences in the spatial domain between analytical and numerical results more quantitatively. To estimate the performance of the theories, the rms error is defined as

$$\epsilon = \frac{\sqrt{\sum_m \sum_n |\Phi_{m,n} - \tilde{\Phi}_{m,n}|^2}}{\sqrt{\sum_m \sum_n |\Phi_{m,n}|^2}}, \quad (4)$$

where $\Phi_{m,n}$ and $\tilde{\Phi}_{m,n}$ represent the pixel intensity of the exact solution and approximations, respectively. With the above definition, for both polarizations, the rms errors are 0.6% and 1.5% for the PO and first order SSA images, respectively. The error estimation shows that approximate theories such as PO and SSA for moderate height surfaces can predict the overall scattering events quite accurately.

B. Large height surface

For the moderate rms height case only single scattering contributions were observed. However as the surface rms height increases some additional effects can appear. Figure 3 shows radar images from the exact MOM solution for the scaled large rms height surface ($\sigma = 2.0$ cm). When compared

to the moderate rms height case, the maximum pixel amplitudes (-3.41 dB for HH and -3.47 dB for VV) are decreased by approximately 2.2 dB due to the fact that the moderate height surface has more specular points than the large height surface. Images for both polarizations show additional scattering points below the surface, possibly from multiple scattering effects.

To study the origin of these additional scattering points, a ray tracing analysis was carried out to predict the locations of points which occur due to double reflection. Figure 4 illustrates predicted locations corresponding to double bounces between two points. Overlaid by the images of Figure 3, the predicted points match the time-delayed images from multiple scattering effects. Another property of the multiple scattering images is that the spots are deformed into stripe-like images with an increasing angular bandwidth whereas single scattering spots become more focused. These effects were clearly observed when the angular bandwidth was doubled from 20° to 40° .

First order SSA predictions for the large rms height surface are presented in Figure 5 and fail to resolve the non-local interactions. However, good results for single scattered responses are obtained when compared to the MOM images of Figure 3. PO images (maximum pixel amplitude of -3.43 dB for HH and -3.42 dB for VV) are again virtually identical to the first order SSA (maximum pixel amplitude of -3.49 dB for HH and -3.53 dB for VV) for this case, and maximum pixel amplitudes from both theories are within 0.1 dB of the maximum pixel amplitude for numerical results in both polarizations. PO images produce an rms error of 4.4% for HH and 6.8% for VV while first order SSA images obtain an rms error of 4.9% for HH and 6.8% for VV in the image domain, respectively, which are larger than the moderate rms surface case. This is expected because both the PO and SSA predictions should be more accurate for surfaces with smaller slopes.

Non-local SSA (NLSSA) images are also presented in Figure 5. Excellent predictions for single scattering are acquired from NLSSA for both polarizations. More importantly, the NLSSA also captures multiple scattering contributions in VV polarization successfully. Again, the maximum pixel amplitude (-3.42 dB for HH and -3.46 dB for VV) shows less than a 0.1 dB difference from MOM/FB results, and the rms error is reduced to 4.1% and 2.1% for HH and VV, respectively. Unlike the first order SSA, NLSSA produces a smaller rms error for the VV case because NLSSA is able to capture multiple scattering effects comparable to the level of the MOM. For the HH case, however, the NLSSA underestimates multiple scattering effects. Changing the windowing function

to a lower side-lobe windowing such as the Nuttall window (3 cosines), multiple scattering points can also be observed in the NLSSA HH case. The underprediction of HH multiple scattering effects observed is consistent with the discussion of polarization effects in multiple scattering NLSSA contributions provided in [16].

C. Oblique incidence images

Figure 6 shows images from MOM and NLSSA results for aspect angles centered at 45° for the large rms height surface. With a 20° angular bandwidth, the highest incident angle becomes 55° . The incident field propagates in the $+x$ and $-z$ directions in the images shown. When compared to the normal incidence case, scattering centers have moved to points near the specular direction at 45° , and the maximum pixel amplitude is -7.58 dB for HH and -7.45 dB for VV. Images formed with the moderate height surface show similar features and a maximum HH and VV pixel amplitudes of -31.8 dB and -31.5 dB, respectively. Because rms slopes for the moderate and large height surfaces are 13.28° and 20.66° , respectively, the probability of obtaining specular features at 45° incidence angle is much greater for the large height surface, resulting in the much larger maximum pixel amplitudes compared to the moderate height case. Overall scattering cross sections for the moderate height surface are primarily non-specular in this angle range, and thus decrease rapidly as the angle increases. At high incidence angles multiple scattering events are no longer observable for the large height surface although the exact images show a very low level of contributions when the dynamic range is extended. This is because the chance to have near specular reflections for two points simultaneously reduces significantly for smooth Gaussian roughness surfaces and, thus dominant scattering mechanisms are from the specular points.

Performance of the approximate theories for the large height surface is as follows: PO (1.6% error, -7.45 dB maximum), SSA (1.6% error, -7.45 dB maximum), NLSSA (5.7% error, -8.1 dB maximum) in HH, while VV performance is: PO (0.5% error, -7.43 dB maximum), SSA (9.0% error, -6.66 dB maximum), NLSSA (23.9% error, -5.5 dB maximum). For the moderate height surface case, performance is: PO (2.8% error, -31.6 dB maximum), SSA (1.8% error, -31.7 dB maximum), NLSSA (4.9% error, -32.3 dB maximum), in HH, while VV performance is: PO (0.64% error, -31.5 dB maximum), SSA (13.9% error, -30.3 dB maximum), NLSSA (21.6% error, -29.96

dB maximum). Errors obtained in HH polarization for both surfaces are comparable to those at normal incidence, although the NLSSA shows slightly worse performance compared to PO and SSA results. Vertical polarization results however show greatly increased errors for the NLSSA and SSA theories, while PO continues to perform well. This somewhat surprising result suggests that the large height surface is sufficiently rough to begin to approach the geometrical optics (GO) limit, in which scattering is completely dominated by specular points. The similarity of HH and VV maximum pixel amplitudes from the MOM/FB model further indicates a GO scattering behavior. Since GO results are captured by the PO theory, but only approximately by the SSA and NLSSA theories as more terms are included, the low order SSA and NLSSA methods used here obtain somewhat larger errors. Of course, generalization of these results will require further image studies of a larger number of surface realizations.

4 Summary and Conclusion

Backscatter radar images of a deterministic rough surface with a Gaussian spectrum have been investigated. Observations in the image domain enabled interpretation of the major and secondary scattering events on the rough surfaces. Dominant scattering events were found at surface points related to the near specular directions.

For the moderate rms height surface ($\sigma = 1.25$ cm and $l_c = 7.5$ cm) single scattering returns are dominant and multiple scattering effects were negligible at normal incidence. In this case, PO and first order SSA predictions showed excellent agreement with numerical results for both horizontal and vertical polarizations. Estimated image domain errors between PO, first order SSA, and numerical images were less than 2%.

Multiple scattering effects at normal incidence were found to become more significant as the rms height increased, as depicted in the numerical images. For the large rms height surface with $\sigma = 2.0$ cm and $l_c = 7.5$ cm, time delayed spots due to multiple scattering clearly appeared on the image space underneath the surface. A simple ray tracing algorithm was able to specify the location of these spots due to double reflection between two points. Images revealed that multiple scattering effects were captured successfully from the lowest order NLSSA results, especially in

VV polarization, but not from the PO or the first order SSA results which emphasize only single scattering and local interactions.

The studies of this paper demonstrate that radar images provide a means for better understanding of rough surface scattering problems, and confirm that the NLSSA can capture some multiple scattering effects.

Acknowledgements:

Use of the RIDE imaging code provided by Dr. I. J. Gupta of the ElectroScience Laboratory is appreciated. This work was sponsored by ONR contracts N00014-97-1-0541 and N00014-00-1-0399, and NSF project ECS-9701678.

References

- [1] L. Tsang, J. A. Kong, and R. T. Shin, *Theory of Microwave Remote Sensing*, Artech House, 1985.
- [2] J. T. Johnson, R. T. Shin, J. A. Kong, L. Tsang, and K. Pak, "A numerical study of the composite surface model for ocean backscattering," *IEEE Trans. Geosc. Rem. Sens.*, vol. 36, pp. 72–83, 1998.
- [3] G. Zhang and L. Tsang, "Wave scattering and scene image of trees generated by Lindenmayer systems," *Proc. Int. Geosci. Remote Sensing Symp.*, Lincoln, Nebraska, pp. 728–729, 1996.
- [4] H. Kim, J. T. Johnson, and B. Baertlein, "High resolution Ka-band backscatter images of a small tree: Measurements and models," *IEEE Trans. Geosc. Rem. Sens.*, pp. 899–910, Mar. 2000.
- [5] S. Brown and J. C. Bennett, "High-resolution microwave polarimetric imaging of small trees," *IEEE Trans. Geosc. Rem. Sens.*, vol. 37, pp. 48–53, Jan. 1999.
- [6] J. Fortuny and A. J. Sieber, "Three-dimensional synthetic aperture radar imaging of a fir tree: first results," *IEEE Trans. Geosc. Rem. Sens.*, vol. 37, pp. 1006–1014, Mar. 1999.
- [7] S. E. Shih, K. H. Ding, Y. Zhang, and J. A. Kong, "Subsurface detection based on enhanced SAR signatures using angular correlation function," *Proc. Int. Geosci. Remote Sensing Symp.*, Seattle, WA, pp. 530–532, 1998.
- [8] G. Zhang and L. Tsang, "Application of angular correlation function of clutter scattering and correlation imaging in target detection," *IEEE Trans. Geosc. Rem. Sens.*, vol. 36, pp. 1485–1493, Sep. 1998.
- [9] H. Kim and J. T. Johnson, "A comparison of rough surface scattering theories at low grazing angles," *Proc. URSI*, Toronto, Canada, p. 196, 1999.
- [10] A. G. Voronovich, "Small-slope approximation in wave scattering by rough surfaces," *Sov. Phys.-JETP*, vol. 62, pp. 65–70, 1985.
- [11] A. G. Voronovich, "Small-slope approximation for electromagnetic wave scattering at a rough interface of two dielectric half-spaces," *Waves Random Media*, vol. 4, pp. 337–367, 1994.
- [12] A. G. Voronovich, *Wave Scattering from Rough Surfaces*, Springer Series on Wave Phenomena 17, 1995.

- [13] S. L. Broschat, "Small slope approximation reflection coefficient for scattering from a "Pierson-Moskowitz" sea surface," *IEEE Trans. Geosc. Rem. Sens.*, vol. 31, pp. 1112–1114, Nov. 1993.
- [14] E. I. Thorsos and S. L. Broschat, "An investigation of the small slope approximation for scattering from rough surfaces. Part I. Theory," *J. Acoust. Soc. Amer.*, vol. 97, pp. 2082–2093, 1995.
- [15] S. L. Broschat and E. I. Thorsos, "An investigation of the small slope approximation for scattering from rough surfaces. Part II. Numerical studies," *J. Acoust. Soc. Amer.*, vol. 101, pp. 2615–2625, 1997.
- [16] A. G. Voronovich, "Non-local small-slope approximation for wave scattering from rough surfaces," *Waves Random Media*, vol. 6, pp. 151–167, 1996.
- [17] S. L. Broschat, "Reflection loss from a "Pierson-Moskowitz" sea surface using the nonlocal small slope approximation," *IEEE Trans. Geosc. Rem. Sens.*, vol. 37, pp. 632–634, Jan. 1999.
- [18] E. I. Thorsos, "The validity of the Kirchhoff approximation for rough surface scattering using a Gaussian roughness spectrum," *J. Acoust. Soc. Amer.*, vol. 83, pp. 78–92
- [19] D. A. Kapp, *A New Method to Calculate Wave Scattering from Rough Surfaces at Low Grazing Angles*, Ph.D. dissertation, Virginia Polytechnic Institute and State University, 1995.
- [20] H.-T. Chou and J. T. Johnson, "A novel acceleration algorithm for the computation of scattering from rough surfaces with the forward-backward method," *Radio Science*, vol. 33, pp. 1277–1287, 1998.
- [21] S. O. Rice, "Reflection of electromagnetic waves from slightly rough surfaces," *Commun. Pure Appl. Math*, vol. 4, pp. 361–378, 1951.
- [22] I. J. Gupta and A. Gandhe, "Radar image editing and data extrapolation," Technical report no. 727723-9, The Ohio State University ElectroScience Laboratory, Apr. 1996.
- [23] D. L. Mensa, *High Resolution Radar Cross Section Imaging*, Artech House, 1991.
- [24] F. J. Harris, "On the use of windows for harmonic analysis with the discrete Fourier transform", *Proc. IEEE*, vol. 66, pp 51–83, 1978.

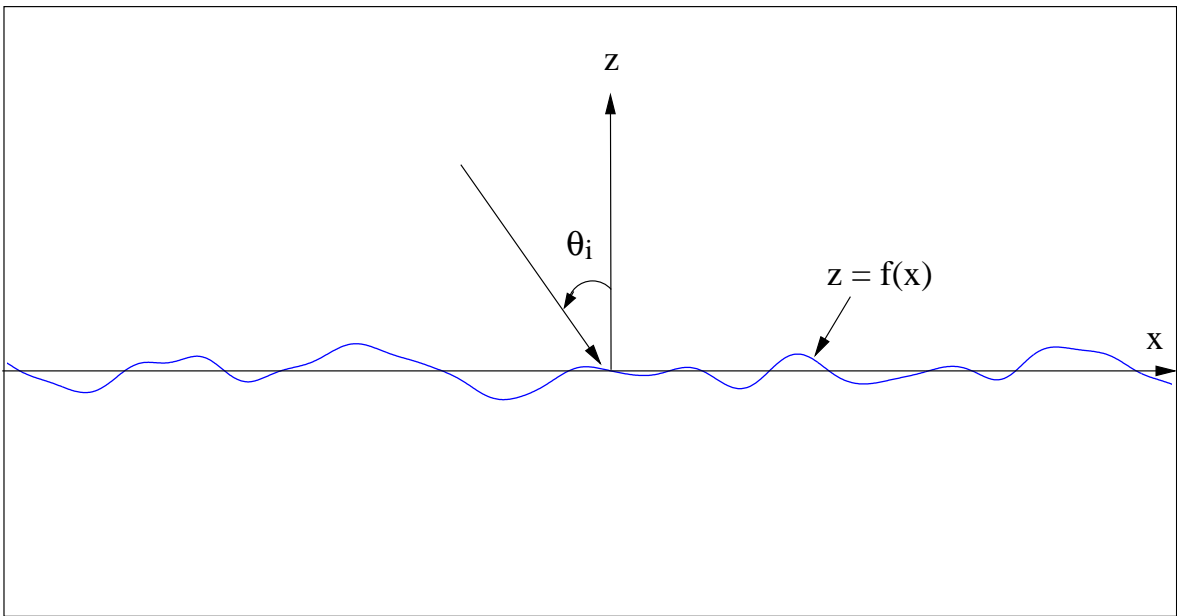


Figure 1: Scattering geometry of a rough surface

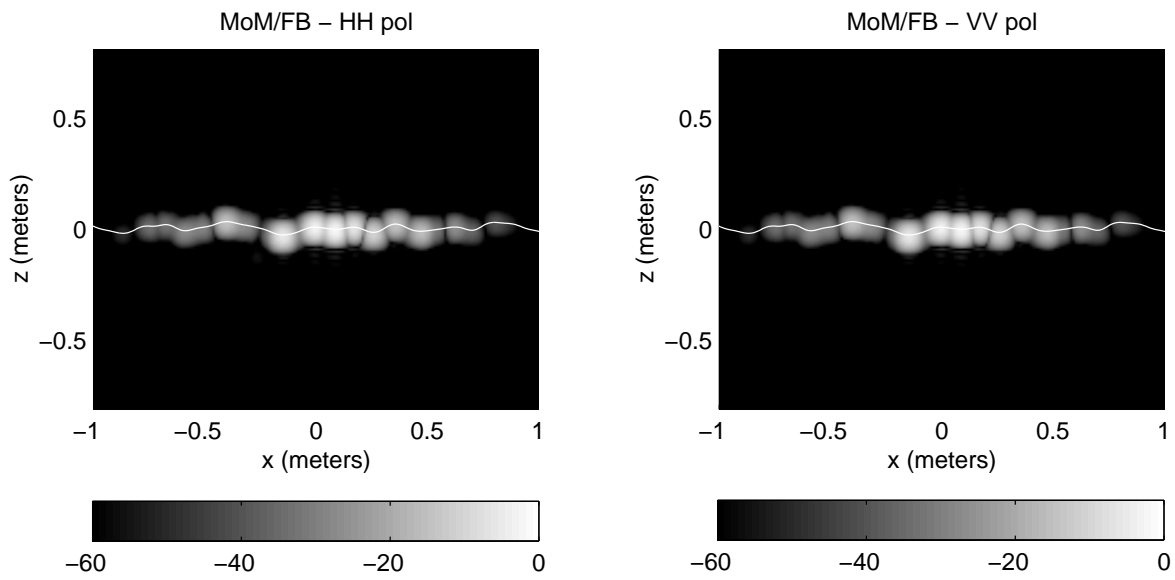


Figure 2: 2-D SAR images for a Gaussian rough surfaces with moderate rms height ($\sigma = 1.25$ cm and $l_c = 7.5$ cm): MOM/FB, $f = 10 \sim 14$ GHz, $\delta f = 50$ MHz, $\theta_i = -10^\circ \sim 10^\circ$ and $\delta\theta = 0.2^\circ$ (a) Horizontal polarization (b) Vertical polarization

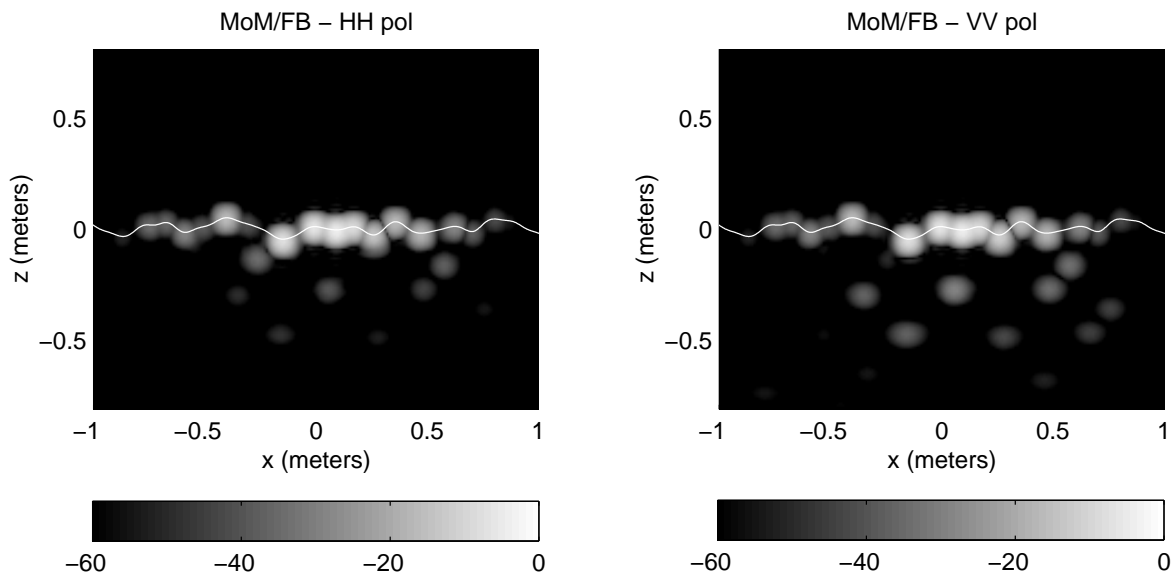


Figure 3: 2-D SAR images for a Gaussian rough surfaces with high rms height ($\sigma = 2.0$ cm and $l_c = 7.5$ cm): MOM/FB, $f = 10 \sim 14$ GHz, $\delta f = 50$ MHz, $\theta_i = -10^\circ \sim 10^\circ$ and $\delta\theta = 0.2^\circ$ (a) Horizontal polarization (b) Vertical polarization

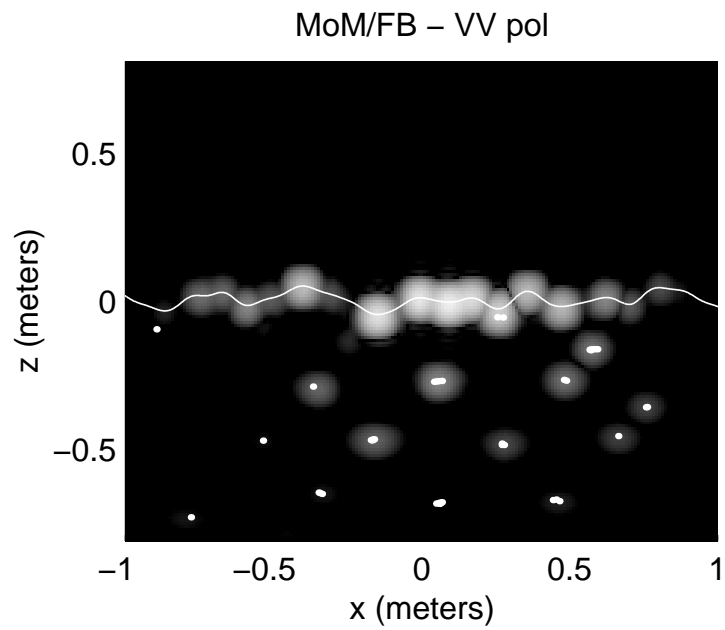


Figure 4: Ray tracing prediction for the location of image spots due to multiple scattering at normal incidence: Overlay of time-delayed scattering centers (marked as dots) and the same image as in Figure 3

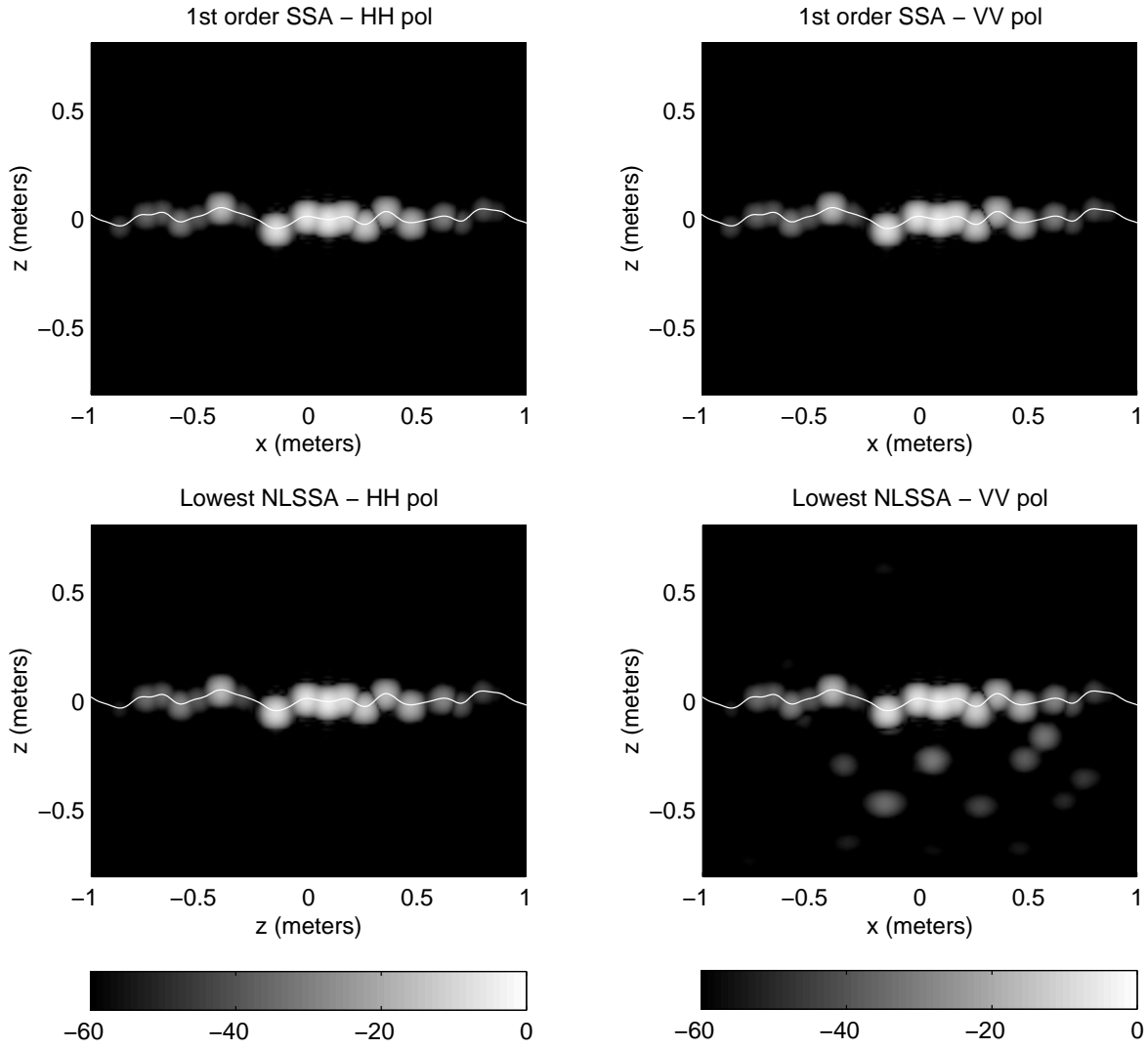


Figure 5: 2-D SAR images of a Gaussian rough surface with high rms height ($\sigma = 2.0$ cm and $l_c = 7.5$ cm): first order SSA and Non-local SSA, $f = 10 \sim 14$ GHz, $\delta f = 50$ MHz, $\theta_i = -10^\circ \sim 10^\circ$ and $\delta\theta = 0.2^\circ$ (a) Horizontal polarization (b) Vertical polarization

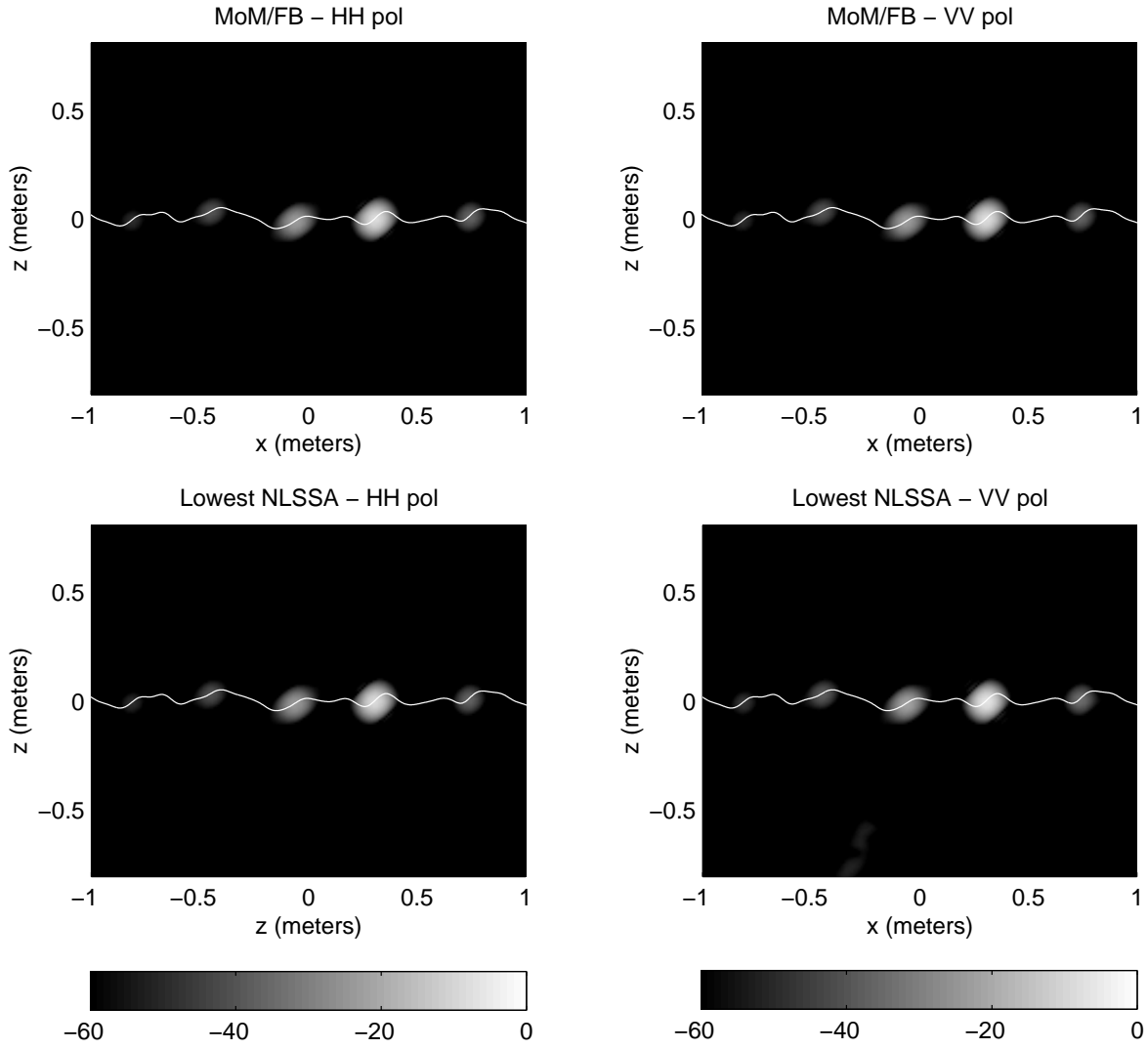


Figure 6: 2-D SAR images for a Gaussian rough surfaces with high rms height and large aspect angles ($\sigma = 2.0$ cm and $l_c = 7.5$ cm): MOM/FB and Non-local SSA, $f = 10 \sim 14$ GHz, $\delta f = 25$ MHz, $\theta_i = 35^\circ \sim 55^\circ$ and $\delta\theta = 0.2^\circ$ (a) Horizontal polarization (b) Vertical polarization